Theoretical considerations of energetics, dynamics, and structure at interfaces[a)]

Uzi Landman, R. N. Barnett, C. L. Cleveland, and R. H. Rast
School of Physics, Georgia Institute of Technology, Atlanta, Georgia 30332

(Received 23 October 1984; accepted 13 November 1984)

We review several of our recent studies investigating the structure and dynamics of two kinds of interfaces: solid–gas and solid–liquid types. For the former, we examine the energetics of some metal–vacuum interfaces and the dynamics of surface diffusion. Metal–vacuum interfaces are studied in the context of pseudopotential theory where the varied contributions to surface energy can be relatively easily categorized and interpreted while still providing quantitative accuracy. We examine the roles of the Madelung energy, surface dipole layer, Hartree energy, and electron response to the relaxation process. While qualitative behavior such as oscillatory multilayer relaxation can be seen even from the simplest "electrostatic" picture, quantitative predictions require both the complete theory and acknowledgment of the full three dimensionality of the system. Results are shown for the (111), (100), and (110) faces of aluminum. In exploring the dynamics of surface diffusion, we discuss a molecular dynamics (MD) simulation of model systems of lead monomers and dimers on a copper (110) surface (where there is a negligible size mismatch between dimer and substrate) and find that dimer diffusion rates can be two to three times those of the monomer. We show typical time evolutions of relevant dimer properties as well as vibrational densities of states and find that a librational or "wagging" mode of dimer motion acts as a "door-way state" for the diffusive jump and associate the elevation of the diffusion rate with its existence. We again employ MD to study solid–liquid interfaces both in equilibrium and under circumstances of rapid melting and recrystallization such as those found during laser annealing. We examine the (111), (100), and (110) faces of a fcc crystal and display profiles versus depth at various times of such properties as number density, temperature, potential energy, and diffusion constant, as well as growth rates. In particular, the close-packed (111) face enjoys a continuous growth process, uniform across the surface and mediated by an extensive interfacial region of liquid layering over the solid, while on the open, "rougher" (110) face the layering is suppressed and growth proceeds laterally across the exposed face in steps.

I. INTRODUCTION

All physical surfaces are in fact interfaces between material systems. The systems connected by the interface may possess several common physical attributes, such as chemical identity, composition, state of aggregation and structure, as in certain solid–solid or liquid–liquid interface systems, or may be of vastly different physical character as in solid–gas and solid–liquid interphase–interface systems. In addition, we distinguish between equilibrium interfaces where all components of the systems are in thermodynamic equilibrium and nonequilibrium interfaces occurring in phase transformations such as crystal growth (from the liquid or gas) or melting. In all cases, the interface region is of finite extent often possessing unique physical characteristics (crystallographical structure, electronic, vibrational and elementary excitation spectra) different from those of the systems connected through it.

Fundamental understanding of the structural and dynamic properties of interfaces is of coupled basic research and technological interest, since often the improvement of technological applications requires knowledge on a fundamental level. The unique structural and dynamical properties of interfaces influence the pathways and rates of physical and chemical processes occurring at interfaces (such as chemical catalysis, corrosion, electrochemical processes, adhesion, electronic and atomic transport, and phase transformations such as crystal growth and melting). In this paper we review recent theoretical studies, performed in our laboratory, investigating the structure and dynamics of two interface systems: solid–gas and solid–liquid types. We have chosen to focus on these systems since in addition to their different nature, exemplifying the richness of interface phenomena, the methods developed and employed in these studies demonstrate different modes of theoretical investigations of interfaces. In Sec. II the energetics underlying the crystallography of certain metal–vacuum interfaces is discussed. Energy pathways and the dynamics of surface diffusion processes are discussed in Sec. III. In Sec. IV we describe molecular dynamics studies of equilibrium crystal–liquid interfaces and of the structure and dynamical evolution of nonequilibrium crystal–liquid interfaces during phase transformations.

II. MULTILAYER STRUCTURAL RELAXATIONS AT METAL–VACUUM INTERFACES

Metal surface structural information is essential for the understanding and elucidation of a large number of surface phenomena. Consequently, major efforts have been devoted

0734-2101/85/031574-14$01.00

in recent years to the development of surface structure experimental probes and their analysis. Progress in the formulation and implementation of theories of structurally predictive capability has been limited, hindered mainly by difficulties in carrying out a self-consistent energy minimization for the coupled system of ions and conduction electrons and the inadequacy of surface relaxation models based on pairwise interaction potentials.[1] Such theories, however, are of great importance since they can provide structural input parameters to be employed in the analysis of data and reveal the nature of the forces (and their relative contributions) which govern the atomic arrangement and in particular structural modifications (relaxation and reconstruction) which are expected (and indeed observed) at the surface region of materials. These observations have led to the formulation[1] of a simple electrostatic model which predicted, semiquantitatively, multilayer surface relaxation in both fcc and bcc materials dependent upon surface crystallographic orientation and other material parameters. The existence of multilayer relaxation phenomena has since been verified by several careful examinations of low energy electron diffraction (LEED) for several systems [e.g., Al(110),[2] Cu(110),[2,3(a)] V(100),[4(a)] Re(01̄01),[4(b)] Fe surfaces[5]]. In this section we review our recently developed theory[6] of lattice relaxation at simple metal surfaces which is based on a *total energy minimization*, provides *quantitative* estimates of metal surface structural parameters and elucidates the nature of forces governing the structure, multilayer relaxation in particular. We illustrate the theory by applying it to the low-index surfaces of Al.

The total energy, E_T, is expressed[6] as the sum of the ground state electron gas energy E_0, the Madelung electrostatic energy, E_M, of point ions in the presence of a semi-infinite negative neutralizing background, the interaction of point ions with the surface dipole layer, $E_{\rm DL}$, and of the Hartree and band-structure contributions E_H and $E_{\rm BS}$, respectively:

$$E_T\{\lambda_n\} = E_0 + E_M\{\lambda_n\} + E_{\rm DL}\{\lambda_n\} + E_H\{\lambda_n\} + E_{\rm BS}\{\lambda_n\}\,. \qquad (1)$$

In our calculation we retain the explicit dependence of the total energy on the crystalline structure. In particular the last four terms depend on layer positions, $z_n^\lambda = (n - \frac{1}{2} + \lambda_n)d$, $n = 1,2,\ldots$, where d is the layer spacing in the bulk and $\lambda_n d$ is the deviation from the truncated bulk location of layer n. E_M and $E_{\rm BS}$ depend in addition on intralayer structure and on interlayer registry ($\Delta\,\mathbf{R}$ will denote the shift in origin of the two-dimensional lattice between adjacent layers, and is characteristic to the exposed face). The total energy is minimized with respect to λ_n, $n = 1,2,\ldots,n_s$.

In the evaluation of the Hartree and band-structure energies we use the local form of the Heine–Abarenkov model pseudopotential:

$$V_P(R,z) = ZV_C(R,z);\quad R^2 + z^2 > r_c^2$$
$$-Ze^2u_c/r_c;\quad R^2 + z^2 \leqslant r_c^2\,, \qquad (2)$$

where $V_C(R,z) = -e^2(R^2 + z^2)^{-1/2}$, Z is the valence, and u_c and r_c are the pseudopotential parameters chosen[7] to fit the bulk compressibility and lattice parameter and used to determine vacancy formation energies [for Al ($r_s = 2.06a_0$) $r_c = 1.388a_0$, and $u_c = 0.3894$].

The dipole layer energy is given by

$$E_{\rm DL}\{\lambda_n\} = Z\sum_n \int d^2R \int dz \times [\rho^e(z) - \rho^+(z)]\,V_C(R,z - z_n^\lambda)\,, \qquad (3)$$

where $\mathbf{R}$ is a $2D$ vector in the surface plane. The Hartree contribution,

$$E_H\{\lambda_n\} = \sum_n \int d^2R \int dz\,\rho^e(z) \times [V_P(R, z - z_n^\lambda) - ZV_C(R,z - z_n^\lambda)]\,, \qquad (4)$$

constitutes together with $E_{\rm DL}$ the first-order correction to the electron–jellium system (E_0) due to the replacement of the positive background by the ionic pseudopotentials. In Eqs. (3) and (4) the background density is denoted by $\rho^+(z) = (3/4\pi r_s^3)\theta(z)$, where $\theta(z)$ is the Heaviside step function, and the ground state electron density in the presence of $\rho^+(z)$ is $\rho^e(z)$. In our calculations, we employ the Lang and Kohn[8] electron density.

In the most primitive model (the PITB model) the system consists of point ions in the presence of a truncated bulk electron density, $E_T\{\lambda_n\} = E_0 + E_M\{\lambda_n\}$. The addition of the dipole layer and Hartree contributions (the DLH model) significantly improves the physical picture and predictive value by including a more realistic description of the inhomogeneous surface conduction electron density and its first-order interaction energy with the ions.

However, the DLH model of surface relaxation (sometimes termed the "frozen profile model") which has been used previously to predict multilayer relaxation[1] does not include the response of the electrons to the presence of the ions. As is demonstrated by our results and their comparison to experimental data, both multilayer relaxation and the full three-dimensional nature of the ionic system must be included in a proper and quantitative treatment of surface relaxation.

The band-structure energy (second order in the pseudopotentials) can be written as

$$E_{\rm BS}\{\lambda_n\} = \frac{1}{2}\sum_{\mathbf{G}}\sum_{n,m} [\exp(i\mathbf{G}\cdot\Delta\,\mathbf{R})]^{n-m} \times \int dz\,\rho_n^\lambda(G;z)W_m^\lambda(G;z)\,, \qquad (5)$$

where $\mathbf{G}$ is the reciprocal lattice vector, and $W_m^\lambda(G;z)$ is the $2D$ Fourier transform of

$$W_m^\lambda(R,z) = V_P(R,z - z_m^\lambda) - \frac{1}{N_A}\int d^2R' \times \int_{(m-1)d}^{md} dz'\rho^+(z')V_C(|\mathbf{R} - \mathbf{R}'|,z - z')\,, \qquad (6)$$

where N_A is the number of ions in a layer. The induced (screening) electron density is linearly related to W_n^λ through

$$\rho_n^\lambda(G;z) = \int dz'\alpha_0(G;z,z')[W_n^\lambda(G;z') + \phi_n^\lambda(G;z')]\,, \qquad (7a)$$

$$\phi_n^\lambda(G;z) = \int dz' g(G;z,z')V_C(G;z - z')\,\rho_n^\lambda(G;z')\,, \qquad (7b)$$

where α_0 is the RPA polarizability and correlation and exchange are included[6] via the local field correction g. The solution of Eqs. (7) is facilitated by using the infinite barrier response model, and by the ansatz $g(G;z,z') = g(G;|z-z'|)^6$.

Including only the $\mathbf{G}=0$ contribution to $E_{\rm BS}$ [Eq. (5)] is equivalent to a one-dimensional treatment of the electron response obtained by averaging the ionic potential over the layers (we denote this one-dimensional electron response model of E_T by DLHBS0, to contrast with the model, denoted by DLHBS, in which the complete $E_{\rm BS}$ is included).

To demonstrate the method, we summarize in Table I results for the surface structures of the low-index faces of Al obtained via minimization of the total energies corresponding to the various models and those obtained by other theories, as well as values obtained from experimental analyses. Percent changes, $\Delta_{n,n+1}$, of the interlayer distance between layers n and $n+1$ from the bulk value, for differing numbers n_s of layers allowed to relax, are given. Inspection of these results and those obtained for other fcc and bcc systems[6,9] shows that relaxation is more pronounced for the open faces, and that multilayer relaxation is essential in all the models and systems considered. We find damped oscillatory relaxations with a period equal to the layer stacking period.

The principal origin of the multilayer oscillatory relaxation lies in the 3D crystallinity of the system; i.e., in the intralayer structure and the registry shift between layers, and in the relaxation between intralayer structure and interlayer spacing. Thus the less open surfaces show smaller relaxations because the ions are more densely packed within the layer, i.e., the resulting potential has less variation both parallel and perpendicular to the surface plane since the layers are neutrally charged (ions plus negative background slab), and because the layer spacing is larger. These effects of crystallinity appear in the Madelung and band structure contributions: the Madelung force between adjacent unrelaxed (100) and (110) layers ($n_R=2$) is attractive while the force between next nearest neighbor layers is repulsive, for (111) surfaces ($n_R=3$) the interlayer forces oscillate with a period of three layers. The Madelung contribution is larger; the band structure terms reduce (screen) the Madelung interactions, but since the electron response is affected by the presence of the surface, this screening is complicated and gives rise to forces which are not simply related to the interlayer distances.

The dipole layer and Hartree energy terms also give rise to oscillatory forces on the layers. However, these forces come from single-ion potentials, i.e., potentials which depend on the position of an individual ion with respect to the bulk, through the interaction with the jellium electron and positive background densities $\rho^0(z)$ and $\rho^+(z)$ [see also the discussion of single-ion potentials in Ref. 6(a)]. These forces, $F_{\rm DL}$ and F_H, are significant only for the topmost layer and, although they do oscillate due to the Friedel oscillations in $\rho^0(z)$, they approach zero rapidly as the z coordinate of the layer increases. The principle effect of the dipole layer and Hartree contributions is to limit the displacement of the first layer with respect to the bulk.

It is evident that a model in which the ions are treated as point ions (PITB) is a poor approximation, and that the second-order (band structure, $E_{\rm BS}$) effects are small compared

TABLE I. Summary of the surface relaxation results for the low-index surfaces of Al obtained using the PITB, DLH, DLHBS0, and DLHBS models (see the text); available experimental results and the results of other calculations are given in the columns labeled Exp. and Other, respectively. The results are presented as the percent change from the bulk value, $\Delta_{l,l+1}$ of the spacing between the layers numbered l and $l+1$. Negative (positive) values of $\Delta_{l,l+1}$ indicate contraction (expansion) of the layer spacing. n_s is the number of layers which were allowed to relax (the results of other calculations, in the last column, are all for single-layer relaxation).

Model		PITB	DLH	DLHBS0	DLHBS	Exp.	Other
n_s				[Al(100)]			
1	Δ_{12}	-2.1	0.3	1.0	$-.7$		$\Delta_{12}=-7.5$
3	Δ_{12}	-2.4	0.4	1.0	0.0	$\Delta_{12}=0$	(Ref. 12)
	Δ_{23}	0.3	0.0	0.7	-0.0	(Ref. 10)	$\Delta_{12}=-4.6$
	Δ_{34}	-0.0	-0.0	-0.1	-0.0		(Ref. 11)
n_s				[Al(100)]			
1	Δ_{12}	-11	-4	-5	-14		$\Delta_{12}=-15$
4	Δ_{12}	-26	-12	-14	-10	$\Delta_{12}=-8.4\pm0.8$,	(Ref. 12)
	Δ_{23}	15	8	9	4	$\Delta_{23}=4.9\pm1.0$,	$\Delta_{12}=2.0$
	Δ_{34}	-7	-4	-2	-3	$\Delta_{34}=-1.6\pm1.1$,	(Ref. 13)
	Δ_{45}	2	1	2	0	[Ref. (2b)]	$\Delta_{12}=-16$
							(Ref. 11)
n_s				[Al(100)]			
1	Δ_{12}	-0.4	0.8	1.9	1.8	$\Delta_{12}=.9\pm.5$	$\Delta_{12}=1$
3	Δ_{12}	-0.4	0.9	0.7	1.6	[Ref. (2c)]	(Ref. 12)
	Δ_{23}	0.0	-0.1	-0.1	0.1	$\Delta_{12}=2.5$	$\Delta_{12}=-1.6$
	Δ_{34}	-0.0	0.0	0.1	0.0	(Ref. 10)	(Ref. 11)

to the first-order (Hartree, E_H) effects. However, while certain qualitative features are revealed by the electrostatic model, from the comparison of the results obtained via the various models with values extracted from experimental data [see Table I, and results obtained recently[9] for the Pb(110) surface in agreement with the analysis of ion backscattering data], we conclude that *quantitative* structural predictions require a minimization of the complete total energy expression [Eqs. (1) and (5)] which retains the full three-dimensional nature of the system, i.e., the DLHBS model. In particular, employment of the one-dimensional electron response, DLHBS0 model, does not yield adequate results.

In the above discussion we have limited ourselves to surface structural relaxations in the normal direction (i.e., variations in interlayer spacings). In investigations of the structure of high-index surfaces of fcc and bcc materials,[6(c)] we have further allowed variations in interlayer registry, with no change of the intralayer two-dimensional unit cell. The results obtained via total energy minimization, using the DLH model, predicted that the less symmetrical surfaces undergo damped multilayer oscillatory registry relaxation [which may be termed (1×1) reconstruction] in addition to multilayer oscillatory relaxation of interlayer spacings. In general, the interlayer registry relaxation shifts the first and second layers toward a more symmetric position with respect to each other; however, since the interlayer coupling extends beyond adjacent layers, this is not necessarily true for the deeper layers. Such coupled oscillatory multilayer registry and interlayer spacing relaxations have been found recently[5] in extensive LEED studies of high-index surfaces of Fe, where interesting trends as a function of "surface roughness" have been suggested.

III. ON THE DYNAMICS OF SURFACE DIFFUSION

Diffusion processes on or in the vicinity of surfaces are of importance in many surface controlled, or driven, physical and chemical phenomena. Such phenomena include crystal growth, surface phase transformations, annealing and recovery of damage, faceting, surface and interfacial (grain-boundary) segregation, and chemical processes heterogeneously catalyzed by surfaces.

The nature of current experimental probes[14] limits the temporal resolution with which diffusion processes can be studied. Valuable information about diffusion systems can be obtained via computer dynamical simulation[15–17] which enable investigations on arbitrarily short time scales and refined spatial resolution. In the following we describe our recent molecular dynamics studies[16] of surface diffusion which demonstrate the potential of such theoretical experiments in revealing the microscopic dynamical mechanisms of certain activated processes.

FIM studies of the diffusion of adatom clusters on surfaces have shown that the migration of the clusters proceeds via distinct alternating cluster configurations [most easily observed for diffusion on "channeled" substrates such as the (211) surfaces of bcc solids].[14] Motivated by these observations we have developed[18] a general stochastic theory of diffusion on ideal and defective lattices in which the diffusing system performs transitions over a manifold of internal states, which may correspond to energy levels and/or distinct spatial configurations. Proper analysis of experimental data in terms of such multistate migration mechanisms allows determination of rate coefficients (frequency factors and activation energies) for transitions among the states participating in the migration mechanism thus extending the information content which may be extracted from the data beyond the mere determination of global diffusion coefficients.

A particularly curious FIM observation concerns the diffusion of Re dimers on the (211) surface of tungsten, where the dimer rate of diffusion was found to be over a factor of 5 larger than that of single Re adatoms. The enhanced dimer diffusion was attributed[14] to an incompatibility between the equilibrium distance between the adsorbed dimer atoms and the distance between the cross-channel minima in the adsorption potential surface dictated by the geometrical structure of the substrate. As a consequence, the adsorbed dimer is never found in its natural equilibrium state and this accounts for a decrease in the energy needed to bring the system to a saddle region of the potential surface which may result in a migration event.

In our study we wish to focus on dynamical aspects of dimer diffusion and therefore have chosen the parameters of our system such as to eliminate the geometrical incompatibility. Employing generic 6–12 Lennard–Jones potentials whose parameters (σ and ϵ) were fitted[19] to materials properties we found that for a system of a lead dimer adsorbed in a cross-channeled configuration on the (110) face of copper, no such geometrical mismatch exists. In order to achieve a faithful simulation of the substrate, our simulations were performed on a thick slab consisting of 14 layers (with 70 atoms in each layer) exposing the (110) surface of the fcc copper substrate. The numerical integration of the classical equations of motion was performed using Gears' predictor–corrector algorithm with an integration time step $\Delta t = 0.0075 t_{\mathrm{Cu}}$, where $t_{\mathrm{Cu}} = (M_{\mathrm{Cu}} \sigma_{\mathrm{Cu}}{}^2/\epsilon_{\mathrm{Cu}}) = 2.9668 \times 10^{-13}$ s (in the following reduced units expressed in terms of the Cu–Cu parameters[19] are used, i.e., distance and energy in terms of σ_{Cu} and ϵ_{Cu}, respectively).

Following equilibration we have performed extensive studies of dimer and single particle diffusion at various temperatures in which we found enhanced dimer diffusion rates (factor of 2–3) compared to the single particle diffusion rates. Since "geometrical mismatch" is absent in our system (by construction) we have set to investigate the origin of the observed enhancement (which as we will demonstrate in the following is dynamical in nature).

In Figs. 1(a)–(c), sample trajectories of the system evolution over a time span of $5\times 10^4\,\Delta t$, for a cross-channel adsorbed dimer, calculated at reduced system temperature (in units of ϵ_{Cu}) $T^* = 0.2$ (corresponding to 2/7 of the substrate melting temperature), are shown. In these figures the crosses correspond to time averaged positions of the top layer substrate atoms and the dots are actual instantaneous locations of the atoms comprising the adsorbed dimer as a function of time. A plot of the Pb–Pb bond length as a function of time shown in Fig. 1(d) allows a clear identification of the jump events. We observe that at $t = 0$ the dimer started at a verti-

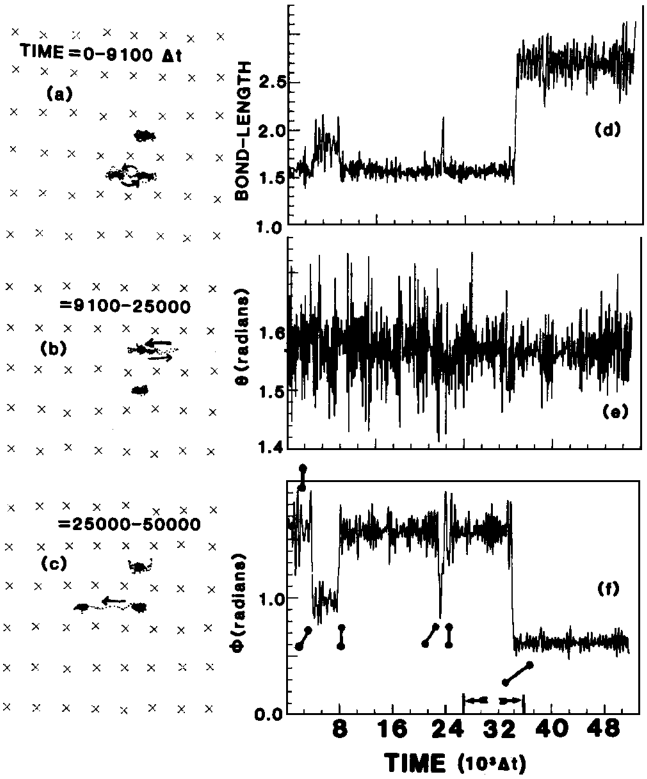

FIG. 1. (a)–(c) Sample trajectories of the system evolution over a time span of $5\times10^4\,\Delta t$, where $\Delta t = 0.0075\,t_{\mathrm{Cu}} = 2.25\times10^{-15}$ s. Crosses indicate averaged positions of the first layer substrate atoms and dots are the instantaneous locations of the dimer atoms. The system was equilibrated with the dimer at a cross channel configuration along the Y direction. (d)–(f) Time evolution of the dimer bond length, out-of-plane angle (θ) between the dimer axis and the normal to the surface, (z) and in-plane angle (ϕ) between the dimer axis and the positive x direction, respectively. Bond length in units of σ_{Cu}. Corresponding dimer configurations are shown in (f).

cal configuration (bond length $\sim 1.5\,\sigma_{\mathrm{Cu}}$). At $t\simeq4\times10^3\Delta t$ the bottom particle migrated to a neighboring site in the channel, returning to the original site at $t\simeq8\times10^3\Delta t$, and so on. Similar information is contained in Fig. 1(f) where the time evolution of the angle ϕ (in radians), the in-plane angle between the dimer axis and the positive x direction, along the channel, is shown, along with the corresponding dimer configurations. A plot of the angle θ, between the dimer axis and the normal to the surface, shows that the orientation of the dimer axis remained almost parallel to the surface plane throughout the course of the sample simulation [see Fig. 1(e)].

To investigate details of the migration mechanism, we focus on the time interval indicated by arrows on the time axis of Fig. 1(f), which spans the time between two jump events culminating in the migration of the bottom adparticle [see Fig. 1(c)]. A closeup view of the variation in the inplane angle ϕ with time is shown in Fig. 2(a). We observe a regular oscillatory variation about the value $\pi/2$ (with frequency $\sim1\times10^{12}\,\mathrm{s}^{-1}$) in time. The amplitude of the dimer libration is modulated, achieving a maximum and decreasing prior to the jump event [marked by an arrow, compare Figs. 1(d) and 1(f)]. In order to interrogate further the type of motion which the dimer is engaged in we show in Fig. 2(b) the equal-time correlation of the x-components of the velocities of the dimer atoms $V_{1x}(t)V_{2x}(t)$. Librational motion in which the two particles move in opposite directions corresponds to a negative value of this correlation function, while a rocking mode in which both particles oscillate in phase yields a positive value. We note that during the increase in the ϕ-oscillation amplitude $V_{1x}V_{2x}$ (as well as $V_{1y}V_{2y}$) takes negative values, while during the decrease in ϕ prior to the jump event a reversal in sign occurs, indicating a change in the nature of the dimer mode of motion. This conclusion is corroborated by the rotational kinetic energy shown in Fig. 2(c) which exhibits a similar sequence. We note also that the same pattern occurs in the time evolution of the adparticle–adparticle bond length [Fig. 2(e)], bond potential energy [Fig. 2(f)], and bond kinetic energy [Fig. 2(g)]. These observations indicate clearly that the librational, out-of-phase motion of the dimer, upon decrease prior to the jump event, exchanged energy with a mode characterized by an in-phase motion of the dimer atoms which did not involve significant vibrations or stretch of the dimer bond. An additional clue to the nature of the prejump mode is provided by a plot of the kinetic energy of the dimer center-of-mass motion as a function of time, given in Fig. 2(h), which exhibits low values while the dimer is librating, and increases in magnitude in coincidence with the noted decrease in the librational motion. Further information concerning the dimer motion is given in Fig. 2(d) which shows the time development of the out-of-plane angle, θ. The oscillations in θ are of a much higher frequency than the in-plane ϕ librational mode and the out-of-plane velocity correlation does not show a clear pattern. In fact, the out-of-plane motion appears rather irregular, while coupled to the in-plane degrees of freedom. Inspection of the time sequences for the dimer particles kinetic energy and dimer total energy (kinetic plus inter-dimer and dimer–substrate potential energies) reveals that the energy content of the dimer increased pursuant to the excitation of the librational mode and remained so until the eventual jump event.

From the above observations we conclude that the evolution of the system leading to the reactive (jump) event is characterized by distinct, though coupled, modes which exchange energy with the substrate and among themselves. The in-phase, rocking mode, which is characterized by a high degree of center-of-mass motion, is coupled directly to the reaction-coordinate (jump event). This mode is excited by the librational mode which preceeds it, whose excitation is caused by coupling to the substrate vibrations and perhaps partially via high-frequency out-of-plane modes (and possibly dimer vibrations), which are orthogonal to the reaction coordinate. The librational mode is therefore identified as the "doorway state" for the reaction.

It is intuitively obvious and rigorously known in the theory of nonlinear oscillators and parametric modulations that the excitation dynamics in such systems depends critically on the frequencies and coupling parameters of the system.[16] To further investigate the activation dynamics and energy pathways in our systems, we calculated the density of vibrational states [Eq. (8a)] and velocity autocorrelation functions [Eq. (8b)], for our system, defined by

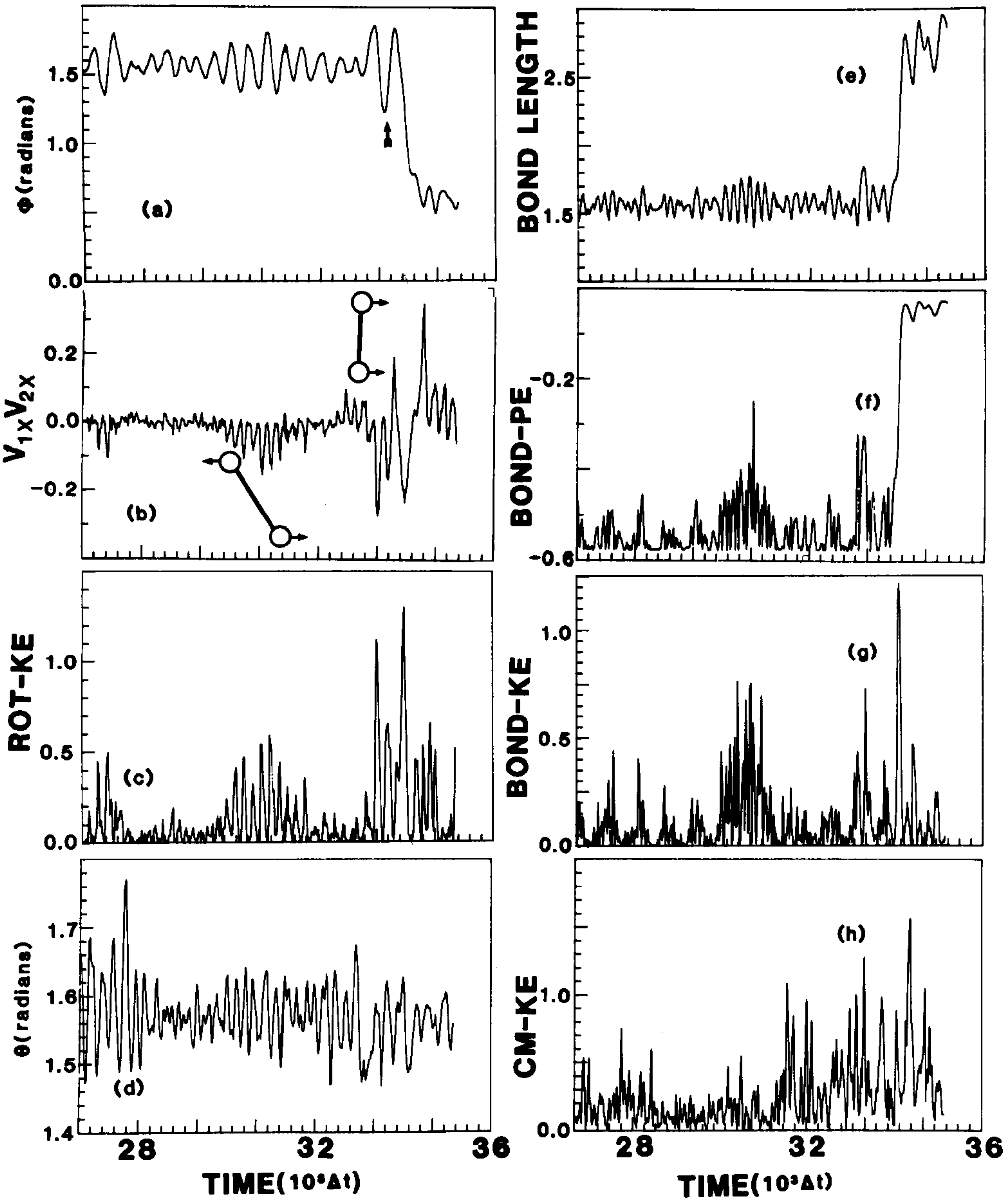

FIG. 2. Time evolution of the angles ϕ and θ [(a) and (d)], are X component of the equal time velocity correlation function $V_{1x}(t)$ $V_{2x}(t)$ in (b), dimer rotational energy (c), dimer bond length (e), bond potential and kinetic energies [(f) and (g)], and dimer center of mass kinetic energy. Energy in units of ϵ_{Cu}, and length in units of σ_{Cu}.

$$\Phi_{A\alpha}(\omega) = \int \Phi_{A\alpha}(t)\cos(\omega t)\,dt; \quad \alpha = x,y,z\,, \tag{8a}$$

$$\Phi_{A\alpha}(t) = \langle A_\alpha(0)A_\alpha(t)\rangle / \langle A_\alpha(0)A_\alpha(0)\rangle\,, \tag{8b}$$

where A is a dynamical variable, and the angular brackets denote averaging over time origins and particles (when applicable). The density of vibrational states for the x, y, and z components of the vibrations of the top-layer atoms of the substrate slab are shown in Figs. 3(a)–3(c), respectively. We observe a marked anisotropy in the vibrational spectrum, which disappears when calculated for deep layers in the slab. This emphasizes the importance of employing a sufficiently extended system in the simulations in order to faithfully represent the dynamics of the system. Components of the velocity autocorrelation functions for motions of the adsorbed dimer atoms, where data have been gathered between jump events, are shown in Figs. 3(d)–3(f). We observe that motion along the surface channel, x [Fig. 3(d)], is of lower frequency than in the normal direction, z [Fig. 3(f)]. In addition, the velocity autocorrelation in the y direction [Fig. 3(e)] is damped rapidly, indicating that motion in this direction is coupled strongly to the substrate, colliding inelastically with the substrate potential (which rises steeply). Finally the velocity autocorrelations for the rate of change of the inplane angle, ϕ, and dimer bond length, r, are shown in Figs. 3(g) and 3(h), respectively. The frequency of the bond vibrations is about double that of the angle variations. Analysis of the dimer modes of motion and their frequencies suggests that the librational mode is excited via direct coupling to the substrate phonons, and to the bond-stretch [see Figs. 3(f) and 3(h)], subsequently channeling energy to the in-phase mode which leads to the jump event. This sequence of activation and energy flow is governed by frequency resonances of the dimer modes with the substrate phonons and by anharmonic couplings. The observed enchancement of the dimer diffusion rate compared to that of single particles is dynamical in

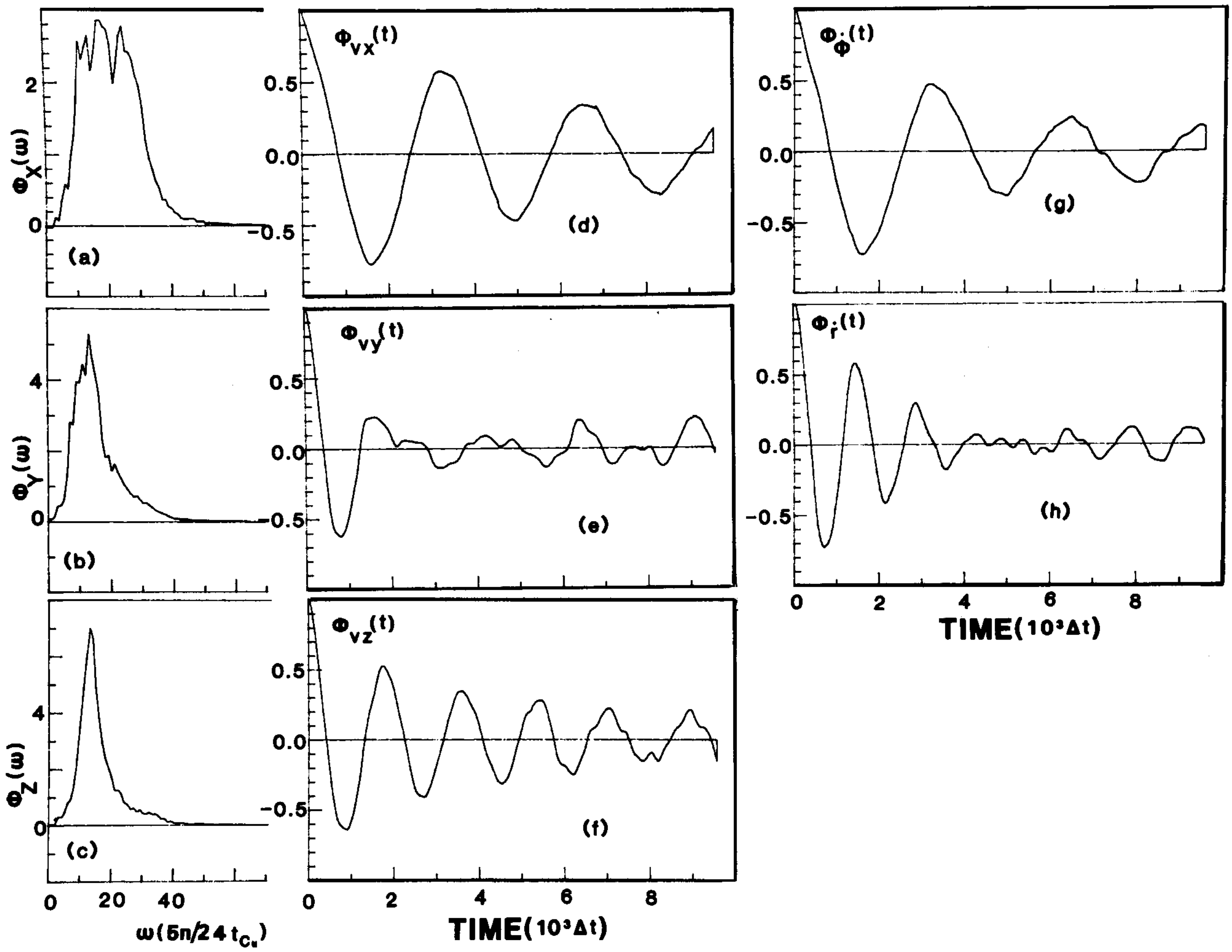

FIG. 3. (a)–(c) Cosine transforms $[\Phi_\alpha(\omega), \alpha = x, y,z]$ of the velocity autocorrelation function for first-layer substrate particles, as a function of ω expressed in units of $(5\pi/24)\ t_{\mathrm{Cu}}{}^{-1} \simeq 2.2 \times 10^{12}$ s. Note anisotropy in the vibrational spectra, which disappears as one moves into the substrate slab. (d)–(f) Velocity autocorrelation functions $[\Phi_{V\alpha}(t) \equiv \langle V_\alpha(0) V_\alpha(t)\rangle / \langle V_\alpha(0) V_\alpha(0)\rangle, \alpha = x, y,z]$ of dimer particles. Data for these correlation functions and those shown in (g) and (h) was accumulated in intervals between jump events. Note the difference in frequency between the x and z modes and the fast damping of the y motion. (g) Autocorrelation function of the angular rate of change, $\Phi_{\dot\phi}(t) \equiv \langle \dot\phi(0)\dot\phi(t)\rangle / \langle \dot\phi(0)\dot\phi(0)\rangle$. (h) Autocorrelation function of the dimer bond, r, rate of change, $\Phi_{\dot r}(t) \equiv \langle \dot r(0)\dot r(t)\rangle / \langle \dot r(0)\dot r(0)\rangle$. Note the higher frequency variations compared to the one shown in (g).

nature, originating from the dimer additional degrees of freedom (bond stretch, libration, and rocking) which provide (resonance) channels to energy flow from the substrate.

While our focus in this study has been on surface diffusion, it is obvious that the concepts which we introduced can be applied in a straightforward manner to other activated rate processes such as desorption and dissociation and perhaps even processes involving energy dissipation such as sticking. Indeed, our present investigations supplement our earlier[20] doorway state model for thermal desorption, in which excitations of the vibrational ladders leading to bond-rupture occurs via coupling of low-frequency nonstretch modes of the adsorbate to substrate phonons. In that case the introduction of the low-frequency doorway modes was necessary due to the frequency mismatch between the frequencies of transitions between low vibrational levels of the bond-rupture stretch mode and the maximum substrate phonon frequency.[20]

IV. ON THE STRUCTURE AND DYNAMICS OF SOLID–LIQUID INTERFACES

The ultrarapid solidification which follows the irradiation of a solid with pulsed laser or electron beams, commonly known as laser annealing, is the basis for the development of novel materials growth and processing techniques and is the subject of current intensive research efforts concerned with the evolution, phase transformations, and properties of nonequilibrium materials systems.[21] Experimental studies of the microscopic mechanisms of excitation and solidification in laser annealing systems are difficult due to the fast rates of the physical processes in these systems, necessitating the development of probes of combined temporal and spatial high resolution. Theoretical progress in understanding the dynamics and kinetics of rapid solidification phenomena is equally challenging due to the highly nonequilibrium nature of these systems and the lack of adequate theoretical methods for the description and analysis of materials under such extreme conditions. Nevertheless, significant progress on both the experimental and theoretical fronts has been realized recently, brought about via the development of novel experimental probes[21] and theoretical simulation and modeling techniques (molecular dynamics,[22] solution of moving boundary coupled heat and matter transport equations,[23] and Monte Carlo studies of kinetic Ising models[24]).

The main theoretical issues encountered in studies of laser annealing systems are (a) the mechanisms of radiation (photons, particles) coupling to solids, (b) nonequilibrium thermodynamics and stability analysis (metastability, morphological stability[25]), and (c) the kinetics and dynamics of phase transformations, i.e., investigations of material processes involving changes in structure, composition, and degree of order. Solidification and melting in general are nonequilibrium phenomena governed by heat and matter transport and kinetic processes at the moving interface between two phases (solid and melt). While the above processes have their origins in particle dynamics, heat and matter transport away from the solidification interface can be described adequately using continuum methods.[23] However, treatment of transport and kinetic processes in the vicinity of the interface requires a microscopic theory, since transport properties in this region are expected to exhibit a marked spatial variation on the atomic scale and interface kinetic processes are inherently of atomistic nature.

Motivated by these considerations, we have developed and performed molecular dynamics simulations[22,26] of model laser annealing systems which allow detailed investigations of the dynamics and structure of solid–melt interfaces and studies of the microscopic mechanisms of melting and rapid solidification. Prior to the discussion of our results we outline certain of the pertinent features of the molecular dynamics simulation method.

A. Model and technique

In molecular dynamics simulations the classical equations of motion for a set of N interacting particles are numerically integrated yielding the positions and momenta (phase–space) of the particles as a function of time.[27] In simulations of bulk materials periodic boundary conditions (pbc's) are imposed thus extending the parallelopiped "calculational cell" (CC) to infinity by an integral number of translations in the three directions which determine the shape and size of the CC. In simulations of systems involving surfaces or interfaces the periodic boundary condition in the direction perpendicular to the surface plane is removed (resulting in a slab) while maintaining the two-dimensional, in-plane pbc's. In addition since the processes of melting and solidification involve changes in volume and in order to allow for possible structural transformations, we have adapted the Parrinello and Rahman[28] constant pressure molecular dynamics by restricting the boundary conditions and dynamical variation to the vectors **a** and **b** defining the basis of the MD calculational cell thus allowing dynamical variations in areal shape and density, along with free dynamical variation in the direction normal to the surface plane.

The slab configuration is useful in studies of thin film systems. However the phenomena investigated by us in this paper involve systems which are semi-infinite, i.e., while our interest is in processes occurring at the surface region, the physical system is of macroscopic extent in the direction normal to the surface. Consequently, we couple the slab to a substrate of the same crystalline structure and composition. The particles of the substrate are static, exerting forces on the dynamic slab particles (within the interaction range of the potential). To assure that the dynamics is followed faithfully for most of the system and in particular in the vicinity of the interface region of interest, slabs of sufficient thickness are employed in the simulation (typically 30–40 atomic layers for the case of interaction potentials whose range of interaction extends over distances of 2–3 layer spacings thus introducing only a negligible perturbation due to the static nature of the substrate). Geometrical data of the systems which we studied is given in Table II. The numbers of dynamical atoms were chosen such that the areas and thicknesses of the systems, exposing the (111), (100), and (110) low-index surfaces of fcc crystals, are as close as possible, thus affording comparative studies.

Since the bulk of the system serves as a thermodynamic reservoir, and since our dynamic slabs are of thickness which assures proper dynamics in the regions of interest, we treat the two slab layers which are most directly influenced by the forces due to the static substrate as a thermal coupling region. Heat exchange with the constant temperature reservoir (T_R) is achieved via extraction of kinetic energy from the slab through scaling of velocities of the particles in the two-layer coupling region. The scaling factor is determined at each integration time step according to the heat conduction equation

$$\frac{dQ}{dt} = K(T(t))A(t)\frac{dT(z,t)}{dz}, \tag{9}$$

where Q is the rate of heat flow, $A(t)$ is the area of the simula-

TABLE II. Geometrical data used in the simulation of the three low-index fcc crystals; a is the length of the cubic unit cell edge.

Property	(111)	(100)	(110)
Dynamic atoms	1512 (27 layers)	1500 (30 layers)	1505 (43 layers)
Static atoms	168 (3 layers)	150 (3 layers)	175 (5 layers)
Layer area	$24.25a^2$	$25a^2$	$24.75a^2$
Layer spacing	$a/\sqrt{3}$	$a/2$	$a/2\sqrt{2}$
Atoms/layer	56	50	35
Dynamic slab dimension	$15.588a$	$15a$	$15.20a$

tion cell, $K(T(t))$ is the temperature dependent thermal conductivity of the material, and $dT(z,t)/dz$ is the thermal gradient (the explicit time dependence of these quantities is denoted). For our choice of substrate material (6–12 Lennard-Jones potential with parameters corresponding to Ar), the experimental[29] $K(T)$ is used in the simulation. The temperature gradient is obtained by via a linear interpolation between the temperature in the coupling region (determined at each time step by averaging the kinetic energies of particles in that region) and the temperature T_R at a fixed point in the reservoir located at a distance of $20a$ from the coupling region (a is the dimension of the conventional unit cell for our bulk fcc system). This model allows studies of the influence of substrate temperature and/or composition on the melting and solidification processes since different substrate materials or temperatures yield different gradients.

The coupling of the incident radiation pulse to the system is simulated via a time-stepwise scaling of particle velocities applied to the free end of the system, has a triangular intensity-versus-time profile, is of 1.6 ps in duration and carries a total energy of 6.3×10^{-5} J/cm^2. In applying the pulse, an absorption profile given by $\exp[0.02\,z/(1\,\text{Å})]$ is used where z (in angstroms) increases in the direction going out from the solid.

In all our studies the material systems consist of two species, 90 at.% of host species α and 10% of initially random substitutionally distributed impurities β. These particles interact via pairwise 6–12 Lennard-Jones potentials:

$$\Phi_{\alpha\beta}(r) = 4\epsilon_{\alpha\beta}\left[\left(\frac{\sigma_{\alpha\beta}}{r}\right)^{12} - \left(\frac{\sigma_{\alpha\beta}}{r}\right)^{6}\right], \tag{10}$$

where r is the distance between the particles, $\sigma_{\alpha\beta} = (\sigma_\alpha + \sigma_\beta)/2$ and $\epsilon_{\alpha\beta} = (\epsilon_{\alpha\alpha}\epsilon_{\beta\beta})^{1/2}$. $\epsilon_{\alpha\beta}$ is the well depth at the equilibrium separation which occurs at $2^{1/6}\sigma_{\alpha\beta}$ (thus the interacting species are characterized in terms of their mass, $m_{\alpha(\beta)}$, their binding energy, and their atomic size), systematic studies of dependencies of the properties of the system upon host and impurity atomic sizes, masses, and binding strengths can be performed by selecting the values of the above potential parameters.

In presenting our results we often used reduced temperature, energy, and time units defined as follows: $T^* = k_B T/\epsilon_{\alpha\alpha}$. Energy is expressed in $\epsilon_{\alpha\alpha}$ units and $t^* = (\sigma_{\alpha\alpha}^2 m_\alpha/\epsilon_{\alpha\alpha})$, respectively. For a host α, with Argon LJ parameters ($\sigma_{\alpha\alpha} = 3.4$ Å, $\epsilon_{\alpha\alpha} = 120$ K and $m_\alpha = 40$ amu), $t^* = 2.16$ ps. The classical equations of motion are integrated using the Gear predictor–corrector method with a time step $\Delta t^* = 0.0075t^*$.

B. Analysis

Integration of the equations of motion yields the phase-space trajectories for the system from which physical properties and their time evolution can be obtained. To facilitate the presentation of our results, we define for any property g_i which depends on the phase-space point $(\mathbf{r}_i,\mathbf{v}_i)$ of atom i located at z_i (with $z = 0$ set at the bottom of the slab and increasing toward the surface) a local density (per unit length) of that property at z by

$$\hat{\rho}_g(z) = \frac{1}{\sqrt{2\pi s}}\sum_i g_i \exp[-(z-z_i)^2/2s]\,. \tag{11}$$

In our calculations a value of 0.126 of the average layer spacing was used for the width parameter s. This allows us to exhibit our results as continuous profiles in the z direction.

We analyze our results in terms of the following quantities:

(1) The particle number density (per length) profiles, $\rho(z)$, are obtained by letting $g_i = 1$ in Eq. (11). All other properties are presented as per particle local densities

$$\rho_g(z) = \hat{\rho}_g(z)/\rho(z)\,. \tag{12}$$

(2) Kinetic energy profiles, KE(z), obtained by setting $g_i = \frac{1}{2}m_i v_i^{\,2}$ in Eq. (11). The temperature is related to KE(z) by $T(z) = (\frac{2}{3})\mathrm{KE}(z)$.

(3) Potential energy profiles, PE(z), obtained by setting $g_i = \frac{1}{2}\Sigma_{j\neq 1}\,\Phi(|r_i - r_j|)$ in Eq. (11).

(4) Planar orientational order parameter profiles $[O_n(z)]$ defined by substituting in Eq. (11):

$$g_m^{(n)} = \frac{1}{W_m}\sum_{j\in nn(m)} W_{mk}\exp(in\theta_{mj})\,, \tag{13a}$$

where

$$W_m = \sum_{j\in nn(m)} W_{mj} \tag{13b}$$

and

$$W_{mj} = \exp[(z_i - z_m)^2/2\sigma_0^2]\,. \tag{13c}$$

In Eqs. (13a)–(13c), $nn(m)$ denotes nearest neighbors to atom m, θ_{mj} is the angle that the "bond" between particles m and j makes with the x axis (in the plane), n is an integer, and the width σ_0 is chosen to be one-half the interlayer spacing for the material. In the figures showing our results, the magnitude of the complex quantity $O_n(z)$ is given. The order parameter $O_n(z)$ measures the degree of particle planar order in an atomic layer which when in the crystalline state possesses n-fold symmetry, i.e., for a perfect fcc crystal at $T = 0$ K, $O_4 = 1$ for the (100) planes and $O_6 = 1$ for the (111) planes. For the (110) planes, $0_4 = 1$ after a scaling of the rectangular two-dimensional unit cell which converts it into a square. From our experience, discernable crystalline order in a layer is associated with $O_n \gtrsim 0.4$ (see Fig. 4). Values of $O_4 < 0.4$ indicate a disordered, liquidlike state.

(5) Diffusion constant profiles ($D(z)$), obtained via the time-velocity autocorrelation function. Here g_i in Eq. (11) is taken as

$$g_i = \int_0^\infty dt\,[\mathbf{v}_i(t)\mathbf{v}_i(0)]\,. \tag{14}$$

Diffusion constant profiles in the normal direction and lateral diffusion constants parallel to the surface plane are evaluated by a proper choice of the velocity components in Eq. (14).

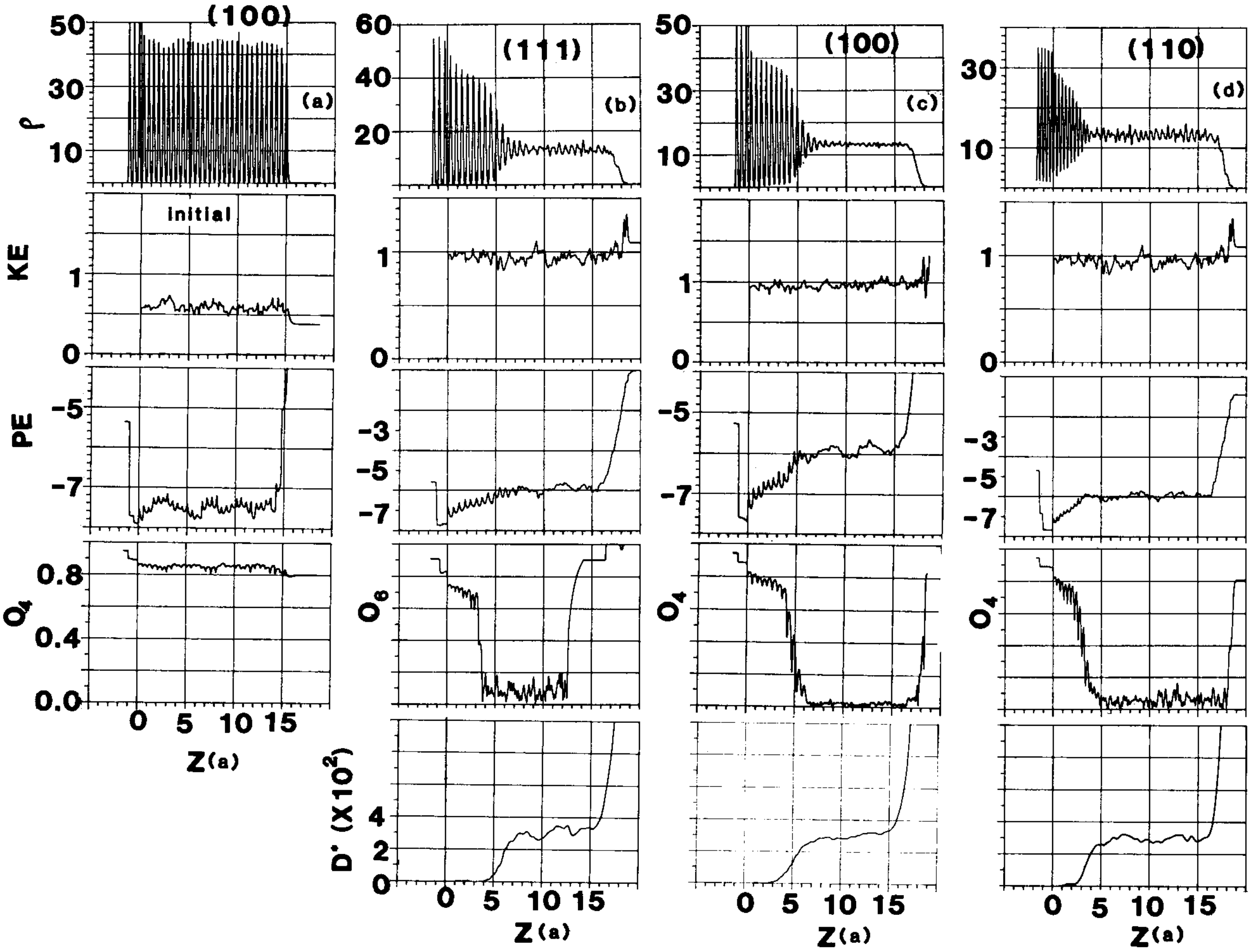

FIG. 4. Number density (ρ), kinetic energy (KE), potential energy (PE), planar orientational order parameter (O_n) and diffusion (D) profiles vs distance Z (in units of a, the cubic unit cell edge length of the bulk crystal, at a reduced temperature $T^* = 0.4$ and zero pressure; at these conditions $a = 5.4$ Å). (a) Profiles for the initial equilibrated (100) system consisting of 90% host particles and 10% random substitutionally distributed impurities (the LJ potential parameters chosen to correspond to Ar as the host and Kr as the impurity). (b)–(d) Profiles of the equilibrium solid–melt coexistence systems, for the three low-index faces of the crystal.

C. Equilibrium solid–melt interfaces

The initial state in all our simulations is an equilibrated fcc crystalline sample composed of 90% host particle with 10% substitutional randomly distributed impurities, at a reduced temperature $T^* = 0.4$, and zero external pressure. We choose

$$\sigma_{\beta\beta}/\sigma_{\alpha\alpha} = 1.07, \quad \epsilon_{\beta\beta}/\epsilon_{\alpha\alpha} = 1.387$$

and

$$m_\beta/m_\alpha = 2.098\,,$$

i.e., a heavier, slightly larger and stronger binding impurity. The three systems which we study differ by the crystal face exposed at the surface (see Table II). Particle number density, kinetic energy, potential energy, and orientational order parameter profiles for the initial state of the (100) systems are shown in Fig. 4(a). The system exhibits sharp atomic layers [$\rho(z)$] with a high degree of inplane crystalline order ($O_4 \simeq 0.8$). Note the variations in the potential energy profile which attains local minima at values of the normal coordinate z corresponding to atomic layers positions.

Having obtained an equilibrated sample a heating pulse is impinged on the surface. The energy thus deposited into the solid serves to disorder and eventually melt a region whose extent depends upon the energy in the pulse and the materials absorption length. Prior to investigations of the resolidification processes, we study properties of the equilibrium solid–melt coexistence systems which are obtained by turning off heat flow to the substrate reservoir during and after the application of the radiation pulse. The system is then allowed to evolve for an extended period of time, achieving the equilibrium state. The equilibrium profiles for the (111), (100), and (110) systems are shown in Figs. 4(b), (c), and (d), respectively. These profiles have been obtained as time averages of the corresponding quantities in the equilibrium state. To simplify comparisons between the results for the three surface systems, distance for all of them is measured in units of a, the cubic unit cell dimension of the bulk crystal at $T^* = 0.4$ ($a = 5.4$ Å).

As seen from these figures, the energy deposited by the pulse melted over half of the samples, producing equilibrium, two-phase, solid–melt coexistence systems. The kinetic energy profiles, KE, shown in Figs. 4(b), (c), and (d), demonstrate the establishment of uniform temperature distributions in the equilibrated systems. The equilibrium (coexistence) temperature corresponding to the average kinetic energy shown in Fig. 4(b), (c), and (d) is $\simeq 0.95T_m$ where T_m is the melting temperature of the pure host system (the slight depression of the melting point is due to the 10% impurities in our systems), at the same conditions. The differences between the solid and melt regions are evident from inspection of the particle number density, potential energy, orientational order, and diffusion constant profiles. Note the distinct, sharp density variations in the ordered solid regions associated with distinct minima in the potential energies and high values of the planar orientational order, in contrast to the behavior and values of these quantities in the melt region.

The solid and melt regions differ also in their dynamical and transport properties as demonstrated by the diffusion profiles shown in Figs. 4(b), (c), and (d). Furthermore, the diffusion profiles exhibit a monotonous, continuous variation over a distance of $\sim 4a$ between the value for the bulk solid ($D = 0$) and that for the bulk of the melt ($D \simeq 0.03$ in reduced units, or 5.37×10^{-4} cm^2/s for Ar potential parameters, which is close to previously determined values[30] using a 6–12 LJ potential and the experimental value (0.033) for liquid argon at the triple point[31]). Anticipating the importance of the solid–melt interface to the nonequilibrium growth dynamics of a crystal in contact with its melt (see Sec. IV D) we focus in the following on the properties of the equilibrium crystal–melt interfaces.

The structure and dynamics of crystal–liquid interface systems have been the subject of increasing theoretical (as well as experimental) interest. Theoretical methods of treating the equilibrium thermodynamics of interfaces in general were introduced by Gibbs in 1878,[32] and much of this seminal work still forms the conceptual framework for research in this field. Most studies aimed towards the development of a molecular theory of equilibrium interfaces are phenomenological in nature. The main difficulty in developing a microscopic theory of the solid–liquid interface (and other liquid interfaces) arises from the presence of the liquid. A satisfactory theory has not yet been developed for the description of homogeneous liquids, although significant progress in this direction has been made, particularly through the advent of numerical simulation methods.[27] The problem of a solid–liquid interface is further complicated since the structural and dynamical properties of the liquid are perturbed by the presence of the solid. The three main theoretical approaches which were developed and applied in investigations of solid–liquid interfaces are: (1) The model approaches[33] which follow and extend the original work by Bernal[34(a)] of the structure of bulk liquids [applied to fcc (111) and hcp (0001) interfaces]. (2) Statistical mechanics theories which employ the liquid-state integral equation methodology in juxtaposition with perturbation theory[35] [applied to fcc (100) and (111) interfaces]. (3) Monte Carlo and molecular dynamics simulation methods[36] [applied to fcc (100) and (111) interfaces]. All three treatments result in a diffuse, layer structured in the liquid, interface. However, the model approaches yield a density deficit at the immediate vicinity of the crystalline surface[33] which is not observed in molecular dynamics simulations. This discrepancy is due partly to the static nature of the crystalline surface in the hard sphere models.

While all the three low-index fcc crystal–liquid interface systems studied by us exhibit a diffuse, layer-structured interfaces [see Figs. 4(b), (c), and (d)], subtle differences due to crystalline face anisotropy should be noted. Due to the diffuse continuous nature of the interface it is difficult to delineate clearly the demarkation separating the solid phase from the melt. We may use the diffusion profiles to guide us in drawing that distinction. It should be noted however that even a moderately defective crystal may exhibit a non-negligible rate of diffusion. In any case, adopting the above criterion it appears that the extent of the diffuse interface is largest for the (100) interface, decreasing slightly for the (111) interface and further decreasing for the (110) interface. Further information is provided by the orientational order-parameter profiles [see Figs. 4(b), (c), and (d)] and via inspection of the corresponding projections of particle coordinates onto the xy surface plane. Upon analysis we find that for the (100) interface intralayer order is changing across the interface transition layer in a gradual manner, as compared to the more abrupt changes occurring for the (111) and (110) interfaces. Note that while the (100) surface possesses fourfold intralayer symmetry, and the (110) can be analyzed using O_4 following the scaling of the two-dimensional unit cell mentioned in Sec. IV B, intralayer order in the (111) crystalline layers is characterized by a sixfold symmetry, O_6, which is a more prevalent packing symmetry in the liquid than the fourfold symmetry. Therefore, the sharp drop in O_6 in Fig. 4(a) is somewhat deceptive.

The crystalline anisotropy of the transition interface region is further demonstrated via the different manners in which the particle densities and interlayer spacings vary across that region for the (111) and (100) interfaces.[37] Analysis of the particle density profiles in Figs. 4(b) and (c) shows that for the (111) system the interlayer spacing remains constant throughout the transition region, equaling roughly that of the crystalline interlayer spacing. The density decrease is achieved for this surface by reducing the number of particles in successive layers. At the (100) interface the interlayer spacing in the transition layer increases gradually from the crystalline value while the number of particles per layer remains constant. These differences between the two interfaces reflect the larger dissimilarity between the bulk liquid structure and the local arrangement in the interfacial liquid layer at the (100) surface, than between the structures of the bulk liquid and interfacial liquid at the (111) surface. At the (100) surface the induced local structure in the liquid in the vicinity of the crystal is octahedral while hard-sphere packing near a flat plane exhibits a nearly perfect two-dimensional hexagonal[34(b)] structure which upon approaching the three-dimensional liquid bulk turns into a polytetrahedral structure of pentagonal symmetry. At the (111) surface the symmetry of the crystalline potential matches closely that of a liquid in contact with a flat wall. The oscillatory behavior of the density profile in the transition region of the (111) interface is then due to the transition between the two-dimensional symmetry of the packing at the immediate vicinity of the crystalline surface and that which occurs in the three-dimensional spherically symmetric bulk liquid.[35]

Finally, we remark upon the similarity in the values of the diffusion constants at the interface regions for the three interfaces studied. Also, we have not found significant differences between the diffusion constants of the interfacial liquid layers in the two lateral directions [although, in the case of the (110) system there seems to be a slight enhancement of the diffusion in the x direction, i.e., along the channels, but this occurs in a region which possesses crystalline, though imperfect, character]. Additionally, we have not found significant differences between the diffusion coefficients at the solid–liquid interface in the lateral and normal to the surface directions. This behavior differs from that which we have found at the liquid–vapor interface and also found recently in molecular dynamics simulations of crystal–vapor interfaces[38] where although no in-plane diffusion anisotropy is observed, the lateral diffusion rate in the topmost liquid layer is significantly larger than the vertical diffusion rate (diffusion in deeper layers is found to be independent of direction), thus demonstrating the difference in particle transport properties at these interfaces.

D. On nonequilibrium crystal–melt interfaces: Melting and rapid solidification

Our initial state is, as before, an equilibrated fcc crystalline sytem exposing one of the low-index faces [see Fig. 4(a) for the (100) case], composed of 90% host particles with 10% substitutional randomly distributed heavier, larger, and stronger binding impurities, at a reduced temperature $T^* = 0.4$ and zero external pressure. The system is then subjected to the influence of a heat pulse of 1.6 ps in duration as described in Sec. IV A, allowing for heat conduction to the substrate reservoir [see Eq. (9)]. A sequence of snapshots of the (100) system evolution at selected times after the end of the heat pulse is shown in Fig. 5. In this figure we show in addition to the number density profiles, the corresponding kinetic energy ($1.5T^*$), potential energy, and planar orientational-order profiles. As seen in Fig. 5(a) 2 ps after the termination of the pulse, the kinetic energy (temperature) of the system is increased and disordering has just started to occur as evident from the PE and O_4 profiles. While the sample is above the melting temperature, not enough time has yet elapsed for significant particle displacements, and for conversion of thermal (kinetic) energy to potential energy. As time progresses the system continues to disorder and melt, with the melting front moving into the interior (to the left in the above figures). Characteristics of the system at the final stages of melting are shown in Fig. 5(b) (25 ps) where about one-half the extent of the system has melted. We notice that the temperature of the melt in the region closer to the vapor side is still well above the melting temperature and that the volume of the system has expanded significantly. In addition, a well-developed diffuse, layer-structured in the melt, crystal–melt interface is observed. At about this time melting stops and resolidification begins, with the solid–melt interface starting to move to the right. As seen in Fig. 5(c), (73 ps) and in subsequent times [Figs. 5(d)–(f)], crystallization started and proceeds while the kinetic temperature of the melt is still above the solid–liquid coexistence temperature. We did not observe any significant degree of supercooling near or at the crystallization front throughout the whole evolution of the system. The moving crystallization front is characterized again by a layer-structured in the melt diffuse interface, possessing density, structural, dynamic and transport properties intermediate between the bulk solid and melt phases connected through it. The final product for all the systems presented in this study is a perfect crystal with a random substitutional impurity distribution.

From the above observations we conclude that the relaxation times which govern the rate at which the layer-structured diffuse solid–melt interface is established under nonequilibrium conditions are extremely short (occurring both during melting and resolidification). The anisotropic "liquid layering," which establishes the material density in the melt region preceding the solidification front, "prepares" the melt for the subsequent evolution of planar crystalline ordering. The unique structural and transport properties of the diffuse solid–melt interface may play an important role in the crystallization kinetics and affect the degree of crystalline perfection and impurity distribution in the resolidified material. We conjecture, that under conditions where the solidification front would be able to advance with a velocity which supercedes that which is necessary for the reorganization of the melt to form the anisotropically structured diffuse interface, a defective, perhaps amorphous, resolidified material would be obtained.

The z location of the recrystallization interface z_i vs time for the three systems is shown in Figs. 6(a)–(c) (this location was determined from analysis of the planar orientational order parameters and analysis of particle trajectories). The crystallization velocities deduced from this data are $v = 7.7$, 10.0, and 8.4 m/s for the (111), (100), and (110) systems, respectively.

Crystal growth from the melt is often discussed in terms of the following mechanisms[40]: (1) Two-dimensional nucleation, where upon nucleation of small monolayer "islands" growth proceeds by further attachment of atoms to the "islands" and spreading of these monolayers across the surface. According to this mechanism the growth rate will be negligibly small for small undercoolings.[40] (2) "Continuous" or "normal" growth,[41] where it is assumed that all atoms arriving at the surface of the solid substrate are able to stick to become solid (thus nucleation is not a necessary kinetic step). According to this mechanism the rate of growth increases with the degree of undercooling, becoming proportional to it for small undercoolings.

Attempts at unifying the two growth modes have been proposed.[42,43] In particular, the model introduced by Cahn assumes that the free energy of the interface is a periodic function of its mean position relative to the lattice periodicity of the solid phase. Thus this model contains the idea of a diffuse (perhaps structured) solid–melt interface.

The two-dimensional nucleation mechanism is expected to be dominant for atomically smooth interfaces while continuous growth is expected to occur on rough surfaces. The plots of the crystalline interface position as a function of time shown in Figs. 6(a)–(c) exhibit different characteristic behavior as we go from the atomically smooth (111) face to the "rougher" (110) face. As seen from these figures, growth on the (111) face is monotonous while at the (110) face it is jag-

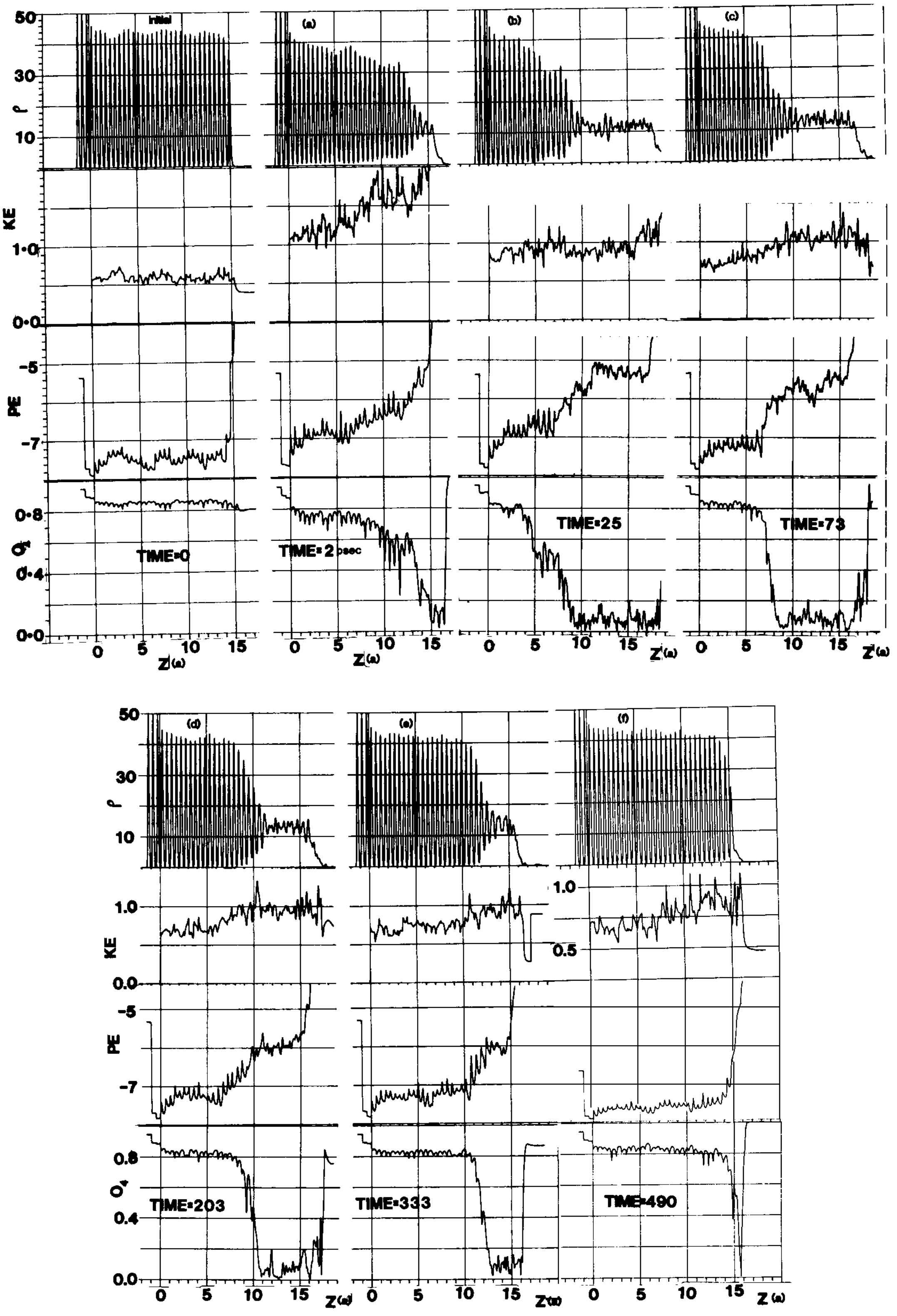

FIG. 5. Profiles of number density (ρ), KE, PE, and O_4 vs Z (in units of a) for the (100) system, at selected times after the termination of the heat pulse. The times (in ps) are given in the figure. Note the melting process in (a) and (b) and the resolidification in (c)–(f).

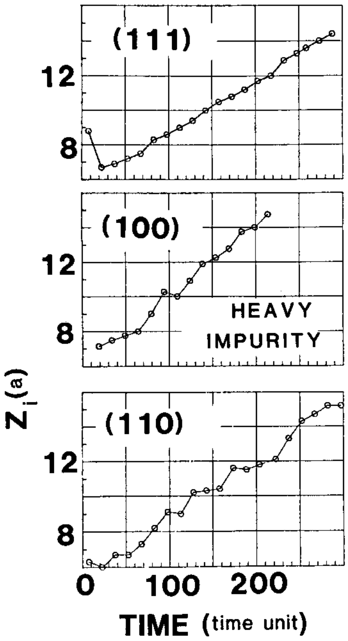

FIG. 6. Interface position z_i (in units of a) vs time (in time units of 2.16 s); (a)–(c) for the heavy impurity systems. The corresponding crystallization velocities are $v = 7.7$, 10.0, and 8.4 m/s for the (111), (100), and (110) systems, respectively.

ged. The difference between the growth modes at these surfaces can be related to the nature of their solid–melt interfaces. As discussed in Sec. IV C, the interface at the close-packed surfaces is of larger physical extent than at the open face (110), exhibiting a more gradual transition between solid to liquid properties. Consequently, growth at the (111) surface involves cooperative ordering over a region in the melt (the diffuse interface) while at the (110) surface it proceeds in a layer by layer fashion. These conclusions are verified by direct observations of the stimulated systems during growth.

Finally, we should emphasize that the observed crystallization velocities in our simulations (and in experiments on rapid crystallization following pulsed laser or electron beam radiation) coupled with the observed negligible degree of undercooling at the interface cannot be analyzed in terms of the conventional models of "continuous" growth. These models are based on equilibrium concepts, employing equilibrium properties and neglect cooperative effects. As we have demonstrated, all of the above assumptions do not hold under conditions of rapid solidification.

[a] Work supported under DOE Contract No. EG-S-05-5489.

[1] U. Landman, R. N. Hill, and M. Mostoller, Phys. Rev. **21**, 448 (1980).

[2] (a) D. L. Adams, H. B. Nielsen, J. N. Andersen, J. Stensgaard, R. Feidenhans'l, and J. E. Sørensen, Phys. Rev. Lett. **49**, 669 (1982); (b) H. B. Nielsen, J. N. Andersen, L. Petersen, and D. L. Adams, J. Phys. C **15**, L1113 (1982) and **17**, 173 (1984); (c) N. B. Nielsen and D. L. Adams, *ibid.* **15**, 615 (1982); (d) J. R. Noonan and H. L. David, Phys. Rev. B **29**, 4349 (1984).

[3] (a) H. L. Davis, J. R. Noonan, and L. H. Jenkins, Surf. Sci. **83**, 559 (1979); (b) H. L. Davis and J. R. Noonan, J. Vac. Sci. Technol. **20**, 842 (1982).

[4] (a) V. Jensen, J. N. Andersen, H. B. Niellsen, and D. L. Adams, Surf. Sci. **116**, 66 (1982); (b) H. L. Davis and D. M. Zehner, J. Vac. Sci. Technol. **17**, 190 (1980).

[5] S. Sokolov, F. Jona, and P. M. Marcus, Phys. Rev. B **29**, 5402 (1984); **31**, 1929 (1985); Solid State Commun. **49**, 307 (1984), where work on multilayer relaxation of layer spacings and registry for Fe(211), Fe(310), and Fe(210) is described.

[6] (a) R. N. Barnett, R. G. Barrera, C. L. Cleveland, and U. Landman, Phys. Rev. B **28**, 1667 (1983); (b) R. N. Barnett, C. L. Cleveland, and U. Landman, Phys. Rev. B **28**, 1685 (1983); (c) R. N. Barnett, U. Landman, and C. L. Cleveland, Phys. Rev. Lett. **51**, 1359 (1983); (d) R. N. Barnett, U. Landman and C. L. Cleveland, Phys. Rev. B **28**, 6647 (1983).

[7] Z. D. Popovic, J. P. Carbotte, and G. R. Piercy, J. Phys. F **4**, 351 (1974).

[8] N. D. Lang and W. Kohn, Phys. Rev. B **2**, 4555 (1970).

[9] J. W. M. Frenken, J. F. van der Veen, R. N. Barnett, U. Landman, and C. L. Cleveland, where experimental and theoretical results for Pb(110) are presented (to be published).

[10] For a recent review on LEED, see F. Jona, J. Phys. C. **11**, 4271 (1978).

[11] M. W. Finnis and V. Heine, J. Phys. F **4**, L37 (1974).

[12] J. P. Perdew, Phys. Rev. B **25**, C291 (1982).

[13] C. Tejedor and F. Flores, J. Phys. F **6**, 1647 (1976).

[14] G. Ehrlich and K. Stolt, Annu. Rev. Phys. Chem. **31**, 603 (1980).

[15] G. De Lorenzi, J. Jacucci, and V. Pontikis, Surf. Sci. **116**, 391 (1982).

[16] U. Landman and R. H. Rast, in *Dynamics on Surfaces*, Proceedings of the 17th Jerusalem Symposium, edited by B. Pullman, J. Jortner, A. Nitzan, and B. Gerber (Reidel, Boston, 1984), p. 215.

[17] H. K. McDowell and J. D. Doll, J. Chem. Phys. **78**, 3219 (1983); J. D. Doll, H. K. McDowell, and S. M. Valone, J. Chem. Phys. **78**, 5276 (1983).

[18] U. Landman, Isr. J. Chem. **22**, 339 (1982); M. F. Shlesinger and U. Landman, *Applied Stochastic Processes*, edited by G. Adomian (Academic, New York, 1980).

[19] T. Halicioglu and G. M. Pound, Phys. Status Solidi (a) **30**, 619 (1975); $\sigma_{\mathrm{Cu}} = 2.338$ Å, $\sigma_{\mathrm{Pb}} = 3.197$ Å, $\epsilon_{\mathrm{Cu}} = 470$ K, $\epsilon_{\mathrm{Pb}} = 2743$ K; $\sigma_{\mathrm{Cu\text{-}Pb}} = (\sigma_{\mathrm{Cu}} + \sigma_{\mathrm{Pb}})/2$, $\epsilon_{\mathrm{Cu\text{-}Pb}} = (\epsilon_{\mathrm{Cu}}\epsilon_{\mathrm{Pb}})^{1/2}$.

[20] G. S. De, U. Landman, and M. Rasolt, Phys. Rev. B **21**, 3256 (1980).

[21] *Laser–Solid Interactions and Transient Thermal Processing of Materials*, edited by J. Narayan, W. L. Brown, and R. A. Lemons (Elsevier, New York, 1983).

[22] C. L. Cleveland, Uzi Landman, and R. N. Barnett, Phys. Rev. Lett. **49**, 790 (1982); Phys. Rev. B (to be published).

[23] R. F. Wood and G. E. Giles, Phys. Rev. **23**, 2923 (1981); R. F. Wood, J. R. Kirkpatrick, and G. E. Giles, *ibid.* **23**, 5555 (1981); R. F. Wood, Phys. Rev. B **25**, 2786 (1982).

[24] G. H. Gilmer, in *Laser–Solid Interactions and Transient Thermal Processing of Materials*, edited by J. Narayan, W. L. Brown, and R. A. Lemons (Elsevier, New York, 1983), p. 249.

[25] J. Narayan in Inst. Phys. Conf. Ser. No. 60, (Institute of Physics, London, 1981), p. 101; A. G. Cullis, D. T. Hurle, H. C. Webber, N. G. Chew, J. M. Poate, P. Baeri, and G. Forti, Appl. Phys. Lett. **38**, 642 (1981).

[26] U. Landman, C. L. Cleveland, and C. S. Brown, Phys. Rev. Lett. **45**, 2032 (1980).

[27] For a recent review, see F. F. Abraham, J. Vac. Sci. Technol. B **2**, 534 (1984).

[28] M. Parrinello and A. Rahman, Phys. Rev. Lett. **45**, 11996 (1980).

[29] I. N. Krupskii and V. G. Manzhelii, Sov. Phys. JETP **28**, 1097 (1969).

[30] A. Rahman, Phys. Rev. **136**, A405 (1964).

[31] J. H. Dymond, J. Chem. Phys. **60**, 972 (1974).

[32] J. W. Gibbs, in *Collected Works* (Longmans, Green, New York, 1928).

[33] A. Bonissent, in *Interfacial Aspects of Phase Transformations*, edited by B. Mutaftschiev (Reidel, Boston, 1982), p. 143.

[34] (a) J. D. Bernal and S. King, *Physics of Simple Liquids* (North-Holland, Amsterdam, 1968), p. 231; (b) J. D. Bernal, Proc. R. Soc. London, Ser. A **280**, 299 (1964).

[35] A. Bonissent and F. F. Abraham, J. Chem. Phys. **74**, 1306 (1981).

[36] For a review, see Ref. 26.

[37] J. Q. Broughton, A. Bonissent, and F. F. Abraham, J. Chem. Phys. **74**, 4029 (1981).

[38] J. Q. Broughton and G. H. Gilmer, J. Chem. Phys. **79**, 5119 (1983).

[39] J. M. Poate, in Ref. 21, p. 263.

[40] D. P. Woodruff, *The Solid–Liquid Interface* (Cambridge University, London, 1973), Chap. 8.

[41] H. A. Wilson, Philos. Mag. **50**, 238 (1900); J. Frenkel, Physik Z. Sovjetunion, **1**, 498 (1932); K. A. Jackson and B. Chalmers, Can. J. Phys. **34**, 473 (1956).

[42] J. W. Cahn, Acta Metall. **8**, 554 (1960).

[43] K. A. Jackson, D. R. Uhlmann, and J. D. Hunt, J. Cryst. Growth **1**, 1 (1967), where a critique of the model suggested by Cahn (Ref. 42) is given.